Catalysis Today 157 (2010) 243–249

Contents lists available at ScienceDirect

Catalysis Today

journal homepage: www.elsevier.com/locate/cattod

In situ studies of titania-supported Au shell–Pd core nanoparticles for the selective aerobic oxidation of crotyl alcohol

Adam F. Lee[a,*], Christine V. Ellis[a], Karen Wilson[a], Nicole S. Hondow[b]

[a] School of Chemistry, Cardiff University, Cardiff CF10 3AT, UK
[b] Institute for Materials Research, SPEME, University of Leeds, Leeds LS2 9JT, UK

ARTICLE INFO

Article history:
Available online 23 May 2010

Keywords:
Bimetallic
Gold
Palladium
XPS
Oxidation
In situ

ABSTRACT

The thermal evolution of titania-supported Au shell–Pd core bimetallic nanoparticles, prepared via colloidal routes, has been investigated by in situ XPS, DRIFTS, EXAFS and XRD and ex situ HRTEM. As-prepared nanoparticles are terminated by a thin (~5 layer) Au shell, encapsulating approximately 20 nm diameter cuboctahedral palladium cores, with the ensemble stabilised by citrate ligands. The net gold composition was 40 atom%. Annealing in vacuo or under inert atmosphere rapidly pyrolyses the citrate ligands, but induces only limited Au/Pd intermixing and particle growth <300 °C. Higher temperatures promote more dramatic alloying, accompanied by significant sintering and surface roughening. These changes are mirrored by the nanoparticle catalysed liquid phase selective aerobic oxidation of crotyl alcohol to crotonaldehyde; palladium surface segregation enhances both activity and selectivity, with the most active surface alloy attainable containing ~40 atom% Au.

1. Introduction

Allylic aldehydes are important fine chemical intermediates [1], and are also used directly as fragrances and flavourings, such as citronellyl acetate (rose/fruity) and cinnamaldehyde (cinnamon) [2]. Their commercial synthesis often proceeds via the selective oxidation (selox) of allylic alcohol analogues, utilising either hazardous stoichiometric oxidants such as Cr^{VI} or peroxides, or expensive homogeneous catalyst systems which are difficult to isolate and recover. In addition to safety considerations, such current technologies are also atom inefficient due to poor selectivity or additional separation/waste treatment steps and therefore economically disadvantageous. Heterogeneous transition metal catalysts afford alternative aerobic selox technologies with great potential safety, process, economic and environmental benefits, however their design and optimisation is hampered by scant knowledge of the fundamental surface chemistry of either allylic alcohol reactants or aldehyde products. The most promising such heterogeneous catalysts are derived from platinum group and noble metal clusters, although these are prone to deactivation. In the case of palladium, time-resolved X-ray photoelectron spectroscopy has shown that product decomposition and associated self-poisoning prevails over model Pd(1 1 1) surfaces [3], with electron deficient palladium sites conferring high activities in allylic alcohol selox [4,5]. Gold addition, via simultaneous/sequential wet impregnation, to form bimetallic Au/Pd nanoparticles (NPs) enhances the activation of diverse (allylic) alcohols, and associated selectivities and lifetimes [6–10]. The origin of this synergy is not well understood, reflecting the relatively poor control that such simple catalyst syntheses offer over the distribution of each metal component, which in turn makes it difficult to derive quantitative structure–activity relations. Our preliminary ultra-high vacuum (UHV) investigations of crotyl alcohol over Pd(1 1 1) model single crystal catalysts [11,12] have shown that alloyed Au improves the surface driven oxidative dehydrogenation to crotonaldehyde (2-butenal) (Scheme 1), one of the simplest allylic aldehydes and an important agrochemical and valuable precursor to the food preservative sorbic acid.

These studies also examined the dependence of (adsorbed and evolved) crotonaldehyde yield upon surface alloy composition, and predicted that ~40% Au should provide the optimal balance between alcohol activation and the undesired aldehyde decarbonylation which dominates over Pd-rich alloys. The goal of the present work is (i) to test the prediction from model single crystals systems that alloyed gold should promote the selective aerobic oxidation of crotyl alcohol to crotonaldehyde during continuous catalytic turnover, and (ii) to establish whether the thermal behaviour and optimal alloy compositions of single crystals under UHV are directly transferable to nanocrystalline catalysts at atmospheric pressure. In order to test this prediction we have synthesised well-defined bimetallic NPs, possessing a thin Au shell surrounding a larger Pd core, dispersed on a high area oxide support to mimic our model

* Corresponding author at: School of Chemistry, Cardiff University, Park Place, Cardiff, UK. Tel.: +44 02920874778; fax: +44 02920874778.
E-mail address: leeaf@cardiff.ac.uk (A.F. Lee).

0920-5861/$ – see front matter © 2010 Elsevier B.V. All rights reserved.
doi:10.1016/j.cattod.2010.04.032

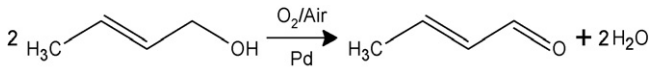

Scheme 1. Catalytic aerobic selective oxidation of crotyl alcohol to crotonaldehyde.

systems. There are several routes to such tailored core–shell nanostructures [13,14], which can provide great insight into the influence of alloying on catalytic chemistry [15]. Here we show how Au shell–Pd core NPs enable us to carefully tune the surface alloy composition of practical catalysts, and thereby tailor their activity and selectivity towards alcohol selective oxidation; optimum performance occurs for a surface Au:Pd atomic ratio = 41:59, in excellent quantitative agreement with predictions from model planar catalyst studies.

2. Experimental

2.1. Catalyst synthesis

Au shell–Pd core/TiO_2 NPs were prepared adopting the methodology of Schmid et al. [16]. Briefly, 16 ml of a H_2PdCl_4 solution (2.68 g/l of Pd) and 1600 ml of water were heated to boiling and treated with 80 ml of a 1% sodium citrate solution, using good mechanical stirring. This mixture was refluxed for 1 h, finally giving a dark grey product. These palladium NPs were diluted with 6000 ml of water, and over the course of 8 h, 1.9 ml of aqueous $HAuCl_4$ (7.44 g/l of Au) and 5 ml of hydroxylamine hydrochloride solution (10 g/l of $HONH_3Cl$) added at room temperature while stirring. The solution lightened and stirring was continued for another 48 h, before addition of 0.2 g of p-$NH_2C_6H_4SO_3Na$ and evaporation of water until the bimetallic nanoparticle began to coagulate. Centrifugation (5000 rpm) yielded a pale grey powder, which was subsequently solubilised in water, dispersed onto P25 titania (Degussa) and evaporated to dryness. Final metal loadings were 0.18 wt% Au and 0.21 wt% Pd. Samples for reactor testing were subsequently heated to temperature (5 °C min^{-1}) within a tube furnace under flowing N_2 (20 ml min^{-1}), held for 10 min and then cooled under inert before screening.

2.2. Catalyst characterisation

Elemental analysis was performed by ICP-MS (MEDAC UK). Powder X-ray diffractograms were collected on a Bruker D8 Advance diffractometer fitted with a LynxEye high-speed strip detector and Cu K_α (154 pm) radiation source. Temperature dependent XRD patterns were acquired in vacuo (10^{-2} Torr) using an Anton Paar HTK 1200 high-temperature environmental cell. Samples were heated at 10 °C min^{-1} to the desired temperature, and equilibrated for 10 min prior to cooling and data acquisition at 50 °C over 2θ = 20–90°, with a 0.02° step size and scan speed of 0.04 $step^{-1}$. X-ray photoelectron spectroscopy (XPS) measurements were performed on a Kratos AXIS HSi instrument equipped with a charge neutraliser and both Mg K_α (1253.6 eV) and monochromated Al K_α (1486.6 eV) sources. Spectra were recorded at normal emission using an analyser pass energy of 80 eV and X-ray power of 225 W. Energy referencing was employed using the valence band and adventitious carbon. Spectra were Shirley background-subtracted and fitted using CasaXPS Version 2.3.15 with a common lineshape based on either an asymmetric Doniach Sunjic profile with FWHM of 2.0 eV (Pd $3d_{5/2}$) and 1.7 eV (Au $4f_{7/2}$), or symmetric Gaussian–Lorentzian mix with FWHM of 2.4 eV (C 1s). Temperature-programmed spectra were recorded within the main analysis chamber using a purpose-built heating stage (thereby obviating the need for sample transfer to a preparation chamber) while maintaining a base pressure of 1×10^{-9} Torr. Samples were heated at 5 °C min^{-1} to the desired temperature, and equilibrated for 30 min prior to cooling to room temperature for analysis. Au L_{III} (11.92 keV) and Pd (24.35 keV) K-edge X-ray absorption spectroscopy (XAS) measurements were made on Station 9.3 of the Daresbury SRS facility in fluorescence mode, using a Si(2 2 0) double-crystal monochromator with a beam current/energy of 150 mA/2 GeV and 9-channel Ortec germanium solid-state detector. Samples were mounted neat within a silica cell under flowing He sample and room temperature spectra recorded before heating at 10 °C min^{-1} to 500 °C for 20 min and re-cooling for ambient data acquisition. Spectra were fitted using the IFEFFIT Open Source software suite for background subtraction, and phaseshift determination and fitting, respectively [17]. Diffuse reflectance FTIR (DRIFTS) was performed with a Nicolet Avatar 370 MCT with Smart Collector accessory and temperature programmable, gold-coated environmental cell interfaced to electronic mass flow controllers via a gas manifold. CO adsorption was conducted under flowing 5 vol% CO/He (20 ml min^{-1}) at room temperature. Samples were first pre-heated to the desired temperature at 10 °C min^{-1} under 20 ml min^{-1} N_2, then equilibrated for 10 min prior to cooling and exposure to CO for 5 min. The cell was purged with N_2 prior to spectral acquisition to eliminate gas phase CO contributions. High resolution transmission electron microscopy (HRTEM) was conducted at the LENNF facility on a FEI CM200 field emission gun TEM running at 197 kV equipped with an Oxford Instruments energy dispersive X-ray (EDX) spectrometer and a Gatan Imaging Filter. Samples were prepared by dispersing in methanol, with a drop placed on a holey carbon coated copper grid.

2.3. Reactor measurements

Alcohol oxidation was performed using a Radleys Carousel Reaction Station equipped with 10 ml reactor tubes. Reactors were charged with 8.4 mmol of crotyl alcohol (Aldrich 99%) in toluene, with mesitylene as an internal standard. Reactions were performed under air at 60 °C with 50 mg of pre-annealed catalyst. Blank reactions were conducted in parallel under identical conditions in the presence of the bare TiO_2 support. Samples were periodically withdrawn for analysis using a Varian CP3800 GC equipped with CP-8400 AutoSampler and DB5 capillary column (film thickness 0.25 mm, id 0.32 mm, length 30 m). Crotonaldehyde was the principal reaction product with butyraldehyde the only by-product, with no side-products attributable to toluene oxidation. Reactions were run for up to 24 h with initial rates determined from the linear portion of the reaction profile. Catalyst selectivity and overall mass balances (closure was >98%) were determined using reactant and product response factors with quoted conversions and selectivities ±2 and ±3%, respectively.

3. Results and discussion

Thermal evolution of the bulk and surface structure of TiO_2-supported bimetallic Au shell–Pd core NPs was first investigated to establish the integrity of the initial Au shell and explore alloying phenomena.

3.1. HRTEM

As-prepared Au shell–Pd core NPs were well dispersed across larger (~100 nm) TiO_2 crystallites, and of uniform size and shape, presenting approximately cuboctahedral morphologies and ranging between 18 and 25 nm in diameter (Fig. 1a). Neither conventional bright field nor HAADF-STEM imaging could provide sufficient localised contrast to unequivocally distinguish the targeted ultrathin Au coating from the underlying palladium cores.

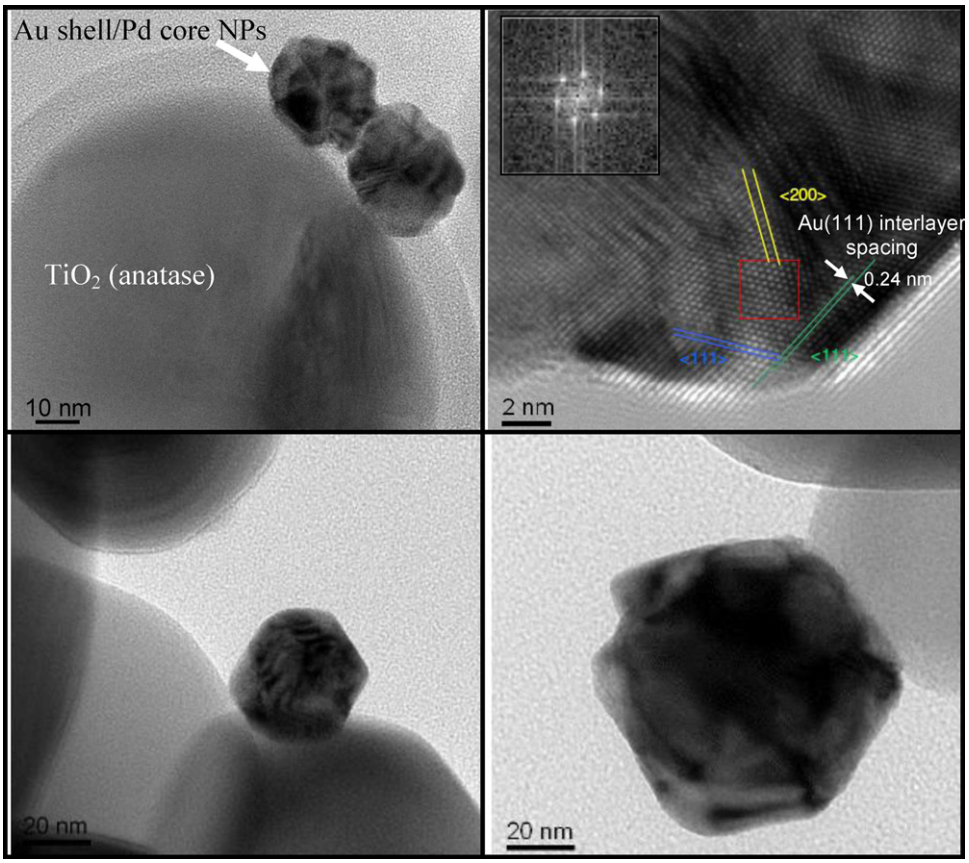

Fig. 1. HRTEM images of (a) as-prepared, (b) atomically resolved as-prepared (Fourier transform inset), (c) 300 °C annealed, and (d) 700 °C annealed Au shell–Pd core/TiO_2 NPs.

However, atomic resolution was achieved through the edge of one nanoparticle (1 1 1) oriented facet, yielding an interlayer spacing of 0.24 ± 0.01 nm (Fig. 1b), in excellent agreement with that observed for pure Au overlayers of comparable thickness grown on a Pd(1 1 1) single crystal [18] and alumina supported Pd core–shell NPs [19], and characteristic of the (1 1 1) spacing of pure gold (0.2355 nm). The analogous, bulk interlayer spacing for a pure Pd(1 1 1) surface is 0.2246 nm [20], significantly smaller than our experimental observation. EDX analysis confirmed the co-existence of both metals, with the average composition of individual NPs 70:30 Pd:Au, in agreement with the molar percentage from elemental analysis (65% Pd), and close to simple geometric predictions for 20 nm Pd nanospheres capped with 5 atomic layers of gold. Annealing $\geq$300 °C induced progressive particle growth (Fig. 1c), which increased up to ~90 nm by 700 °C and was accompanied by increasing surface roughening to yield particle morphologies intermediate between cubeoctahedral and icosahedral (Fig. 1d), strongly reminiscent of those derived from molecular dynamics simulations of annealed Au/Pd alloy NPs [21].

3.2. XAS

The local environment of gold and palladium atoms in the as-prepared core–shell NPs was also probed via EXAFS. Resultant radial-distribution functions are shown in Fig. 2, and in each case fitted well to their characteristic parent monometallic matrices (i.e. only Au–Au and Pd–Pd distances were observed with respective first nearest neighbour bondlengths of 0.285 and 0.275 nm; very close to the expected values for extended fcc gold and palladium structures), indicative of phase-separated metal components in accordance with our desired core–shell structure. This finding is also explicable by the existence of physically separated Au and Pd nanoparticles, however neither were observed in our localised HRTEM-EDX measurements, and the presence of monometallic Pd NPs is entirely inconsistent with our CO DRIFTS titrations, hence

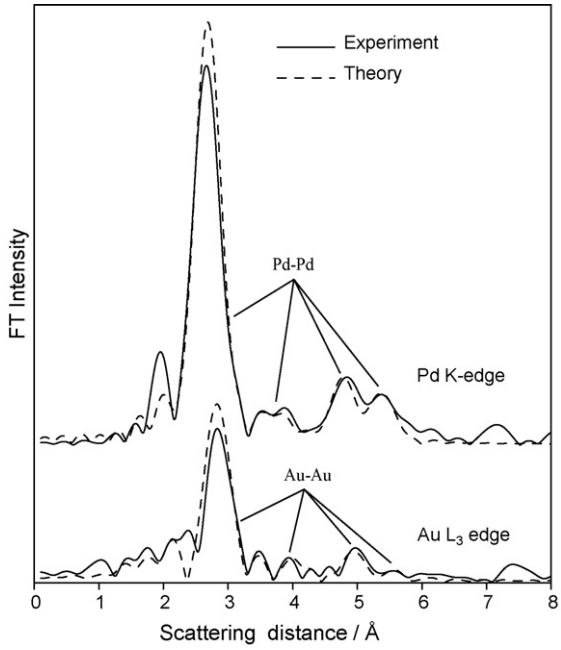

Fig. 2. Fitted radial-distribution functions from Au L_{III} and Pd K-edge EXAFS spectra of as-prepared Au shell–Pd core/TiO_2 NPs.

Table 1
Fitted EXAFS parameters for as-prepared Au shell–Pd core/TiO_2 nanoparticles.

Scatterers	CN1	CN2	CN3	CN4	R1/Å	R2/Å	R3/Å	R4/Å	$\sigma^2$1	$\sigma^2$2	$\sigma^2$3	$\sigma^2$4	R^2
Au[a]–Au	8.4	2.3	7.8	19.3	2.86	4.00	4.97	5.63	0.008	0.009	0.013	0.032	41
Pd[a]–Pd	12	6	24	12	2.75	3.86	4.80	5.41	0.010	0.020	0.021	0.012	30

[a] Excited central atom ≡ Au ($L_{III\text{-edge}}$) or Pd (K-edge).

this possibility can be discounted. The fitted EXAFS parameters (Table 1) are also in good agreement with electron microscopy, with bulk-like Pd–Pd coordination numbers indicating particle diameters ≥20 nm [22,23], and Au–Au 1st and 2nd shell coordination numbers of 8.4 and 2.3, respectively, indicative of a truncated fcc gold phase, as anticipated for a thin capping shell. The absence of Au–Pd distances for the as-prepared material is not surprising when considering the averaging nature of EXAFS. For a gold atom located in a Pd_3 hollow site at the core–shell interface, only 25% of its nearest neighbours are palladium. If the gold shell is 5 layers thick (see Section 3.4), then these interfacial atoms represent only one-fifth of all the Au atoms, with the remainder possessing only Au nearest neighbours. Averaging across the entire shell, as few as 5% of Au atoms are directly coordinated to palladium. In situ annealing the sample to 500 °C under He resulted in the emergence of Pd–Au scattering pairs (Table 2 and Supporting information), demonstrating thermally-induced AuPd alloying, with bondlengths intermediate between those of bulk fcc Pd (0.275 nm) and Au (0.288 nm). The corresponding Pd–Pd distances within the annealed sample are also slightly expanded from those present in the initial palladium core (0.277 nm versus 0.275 nm), as expected following Au dissolution to form a homogeneous Pd-rich alloy.

3.3. In situ XRD

The powder X-ray pattern of the as-prepared core–shell NPs is dominated by reflections from the anatase support, and only exhibit an extremely weak peak ~39.8° indicative of nanometre (>10 nm) sized fcc Pd clusters (Fig. 3). The absence of any pure Au crystallites with long-range periodicity is consistent with gold dispersed as a thin shell across larger Pd cores, although at the low loadings it would have been difficult to detect any pure Au NPs if present. This weak Pd feature remains essentially unchanged up to 300 °C, above which it shifts to lower angle and sharpens, consistent with a simultaneous lattice expansion (see below) and particle growth.

3.4. In situ XPS

Nanoparticle surface compositions were subsequently probed by XPS, and Fig. 4 shows the resulting Pd:Au atomic ratios, using Mg K_α radiation, derived from the Pd $3d_{5/2}$ (335 eV) and Au $4f_{7/2}$ (84 eV) core–hole excitations as a function of in vacuo annealing. Despite the encapsulating Au shell, significant palladium is visible in the as-prepared NPs, resulting in an average surface composition close to $Au_{50}Pd_{50}$. In order to estimate the gold shell thickness, analogous measurements were recorded on the same as-prepared sample using Al K_α radiation, prior to annealing. Different photon energies generate Pd photoelectrons escaping with different inelastic mean free paths (λ), and by comparing the relative Pd intensities obtained on precisely the same sample using these two X-ray sources, it is possible to directly estimate the Au shell thickness (see Supporting information for details of calculation). This technique has the added advantage that reference spectra from monometallic Pd nanoparticles are not required to calculate the shell thickness. For Pd $3d_{5/2}$ photoelectrons, λ_{Pd} = 1.12 nm (Mg K_α) while λ_{Pd} = 1.31 nm (Al K_α) [24]. The experimentally observed Pd XP signal is enhanced by 16% using the higher energy X-ray source, which equates to a 5 atomic layer thick Au shell. Fig. 4 also shows that the surface composition remains unchanged below 400 °C, implying retention of the initial core–shell structure. However, it is

Table 2
Fitted EXAFS parameters for 500 °C annealed Au shell–Pd core/TiO_2 nanoparticles.

Scatterers	CN1	CN2	R1/Å	R2/Å	$\sigma^2$1	$\sigma^2$2	R^2
Pd[a]–Pd	7.4	4.5	2.77	3.88	0.012	0.025	29
Pd[a]–Au	2.6	3.0	2.81	4.00	0.017	0.021	29

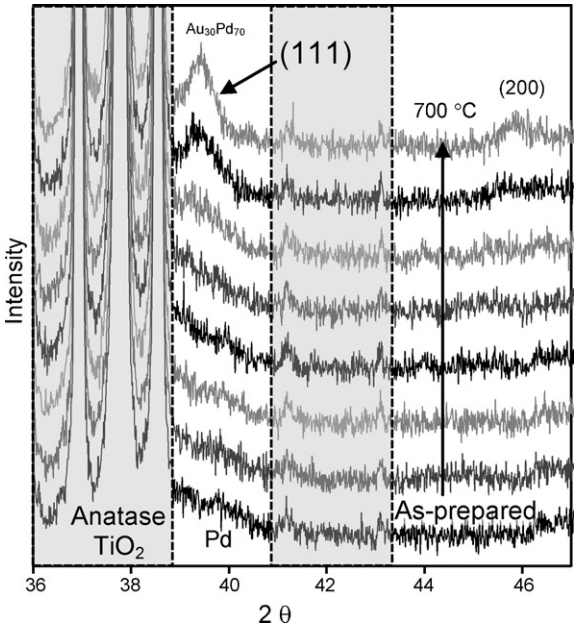

Fig. 3. In situ powder XRD patterns of Au shell–Pd core/TiO_2 NPs as a function of annealing temperature. Reflections arising from the anatase support are shaded out.

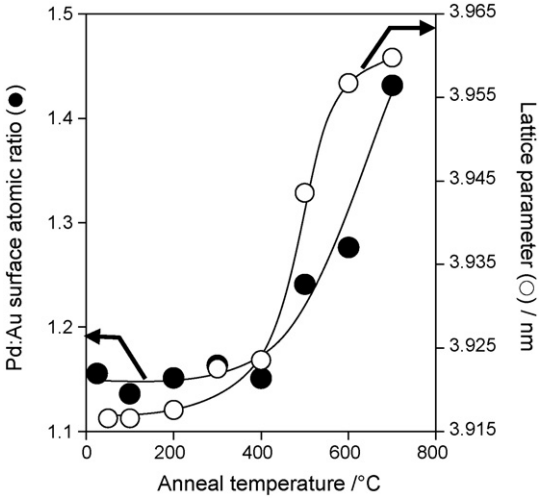

Fig. 4. Surface atomic Pd:Au ratio of Au shell–Pd core/TiO_2 NPs from in situ XPS and bulk lattice parameter from powder XRD as a function of annealing temperature.

important to remember that this surface atomic ratio represents an average throughout the selvedge, and is therefore relatively insensitive to surface segregation (as demonstrated by comparative measurements using LEIS in the Au/Pd(1 1 1) system [25]). Higher temperatures result in a significant decrease in surface Au, indicative of dissolution and transport into the Pd core and supported by the coincident lattice expansion of the metallic (1 1 1) XRD reflection, also shown in Fig. 4, which rises from 0.3917 to 0.3960 nm. Since Au and Pd are fully miscible, the lattice parameter of their pure bimetallic phases can be directly translated into corresponding alloy compositions. This yields a limiting alloy composition of $Au_{35}Pd_{65}$, close to the volume-averaged stoichiometries predicted from ICP-MS and EDX analysis of individual NPs. The final alloy composition in the selvedge is ~40% Au from XPS, the convergence of these values suggesting formation of a homogeneous alloy throughout each nanoparticle. It should be noted that both Au 4f and Pd 3d high resolution XP spectra were dominated by metallic environments, whose binding energies showed respective core-level shifts to lower and higher binding energy (of ±0.3 eV) as previously reported [26,27] during alloy formation at Au/Pd(1 1 1) surfaces. In situ XPS measurements also provide a useful means to assess the thermal stability of the citrate stabiliser employed in synthesising the bimetallic NPs. Although stabilising ligands could influence the resulting catalytic performance, many studies of metal NP catalysts have shown active sites remain accessible for gas and liquid phase reactions despite the presence of adsorbed surfactants or bulky polymer stabilisers [15,28,29] due to the latters' inherent flexibility and intermolecular repulsion which results in surface concentrations well below the monolayer. Indeed it is estimated that as much as 50% of the surface of PVP-stabilised Pt NPs is still available for catalysis [30]. In any event, the temperature-programmed C 1s XP spectra in Fig. 5 reveal that surface citrate ligands (characterised by a high binding energy carboxylate component ~288 eV) thermally decompose by 200 °C. This is below the temperature regime where changes in catalytic behaviour occur (Section 3.6), or where restructuring is detectable by XPS or XRD, hence citrate ligands appear to play a negligible in the chemistry of our Au shell–Pd core NPs.

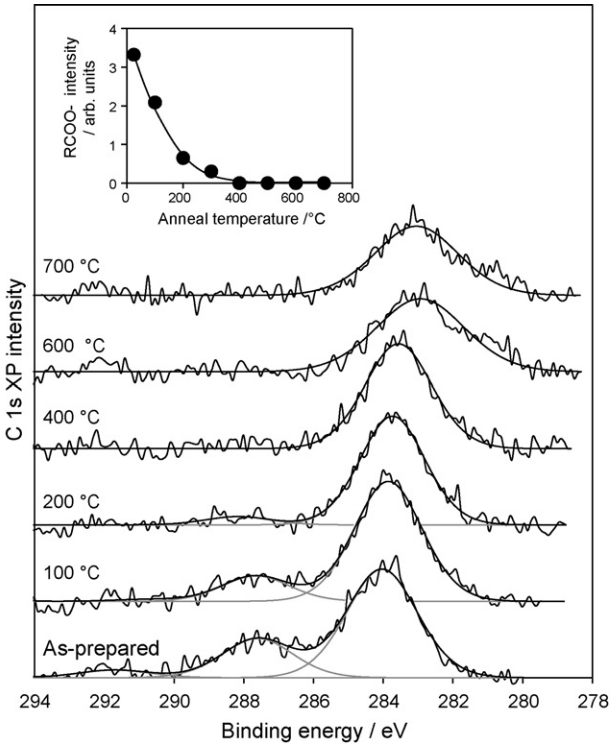

Fig. 5. In situ temperature-programmed C 1s XP spectra of Au shell–Pd core/TiO_2 NPs as a function of annealing temperature. Inset shows integrated intensity of citrate-derived carboxylate component versus annealing temperature.

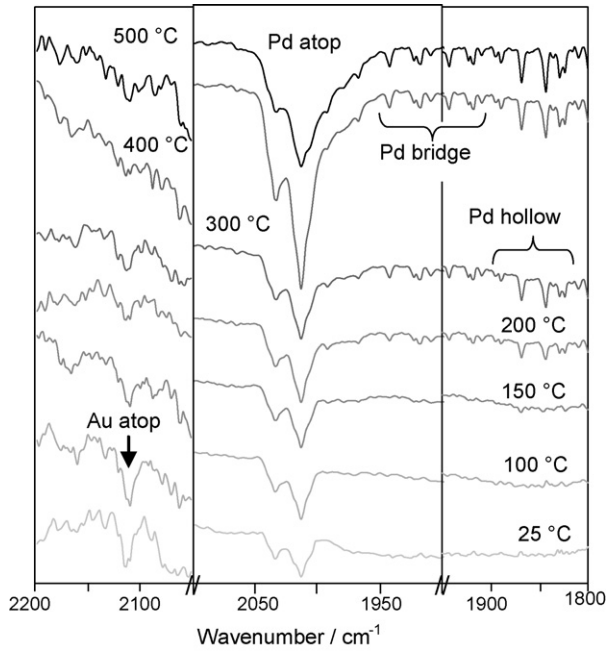

Fig. 6. In situ DRIFT spectra of Au shell–Pd core/TiO_2 NPs exposed to flowing CO at room temperature as a function of pre-annealing temperature.

3.5. In situ DRIFTS

In order to more precisely evaluate the composition of the outermost (most catalytically relevant) surface layer of the core–shell NPs, their chemisorptive properties were also probed via titration with CO. The vibrational frequency of chemisorbed CO is very sensitive to the local surface geometry and electronic structure of AuPd bimetallic systems [26,31], hence DRIFT spectra were recorded in situ as a function of annealing temperature (Fig. 6). Only weak CO adsorption occurred over the as-prepared NPs, giving rise to bands at 2015 and 2035 cm^{-1} which we associate with CO atop palladium, and a feature at 2110 cm^{-1} indicative of CO atop pure gold sites in both continuous gold overlayers and Au nanoparticles [26,32–36]. The absence of bands below 1950 cm^{-1} (characteristic of CO bound in pure Pd bridge or hollow sites) confirms the outermost surface of the as-prepared NPs is free from extended palladium ensembles; we therefore attribute the 2015/2035 cm^{-1} CO stretches to isolated Pd atoms that have surface segregated through the encapsulating gold shell in some of the NPs [37,38]. Annealing strongly suppresses the Au–CO band, while simultaneously enhancing the atop Pd–CO bands and promoting CO adsorption into palladium bridge and hollow sites at 1915/1940 cm^{-1} [38,39] and 1865/1883 cm^{-1} [39]. The temperature dependences of these bands, and the overall amount of chemisorbed CO, are shown in Fig. 7. These trends are entirely consistent with the continuous transformation of Au shell–Pd core into AuPd alloy NPs, and reveal that palladium surface segregation (and concomitant gold dissolution) actually begins as low as 100 °C. This highlights the greater surface sensitivity of CO titration to changes in the terminating layer compared with XPS, although both techniques show that extensive surface alloying requires temperatures >300 °C, in line with predictions from Au/Pd(1 1 1) single crystal studies [11,26,27]. Note the CO DRIFT spectra did not evolve as a function of time under isothermal conditions, suggesting that if

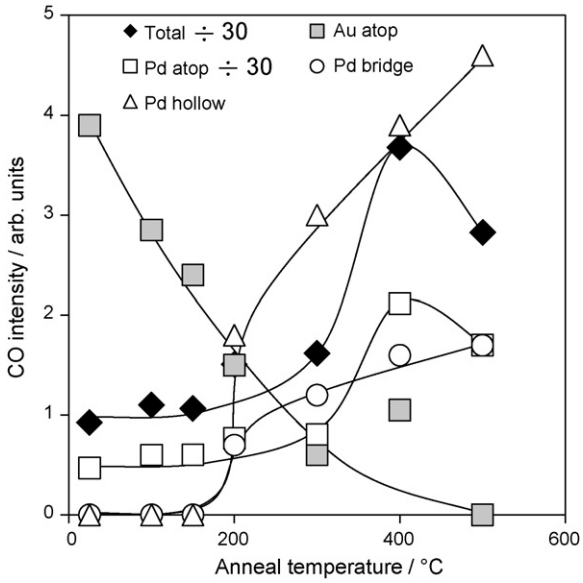

Fig. 7. DRIFTS intensities of principal CO vibrational bands for Au shell–Pd core/TiO_2 NPs as a function of annealing temperature.

CO-induced surface modification occurred, this must be on a faster timescale than our data collection (i.e. <30 s per spectra).

3.6. Crotyl alcohol selox

Having established the successful synthesis of Au shell–Pd core/TiO_2 NPs, and shown that they exhibit controllable surface and bulk alloying upon thermal processing, we finally assessed the impact that such intermixing exerts upon their surface reactivity in liquid phase selox of crotyl alcohol to crotonaldehyde. In contrast to numerous conventional studies, wherein tuning the bulk/surface composition of bimetal catalysts is attempted through synthesising *a series of different catalysts* (for which there is no inherent control over the spatial distribution of each constituent metal and therefore alloy composition achieved), Fig. 8 presents results obtained from a *single well-defined bimetallic catalyst*. It is immediately apparent

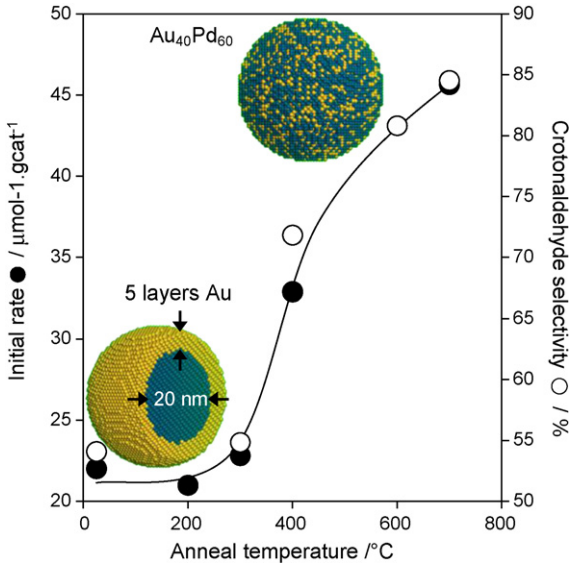

Fig. 8. Surface area normalised, initial rates and selectivities of crotyl alcohol selective aerobic oxidation over Au shell–Pd core/TiO_2 NPs as a function of pre-annealing temperature.

that Au-rich surfaces exhibit poor activity towards crotyl alcohol, in accordance with our recent predictions from ultra-high vacuum measurements on Au/Pd(1 1 1) model catalysts [11,12]. This poor reactivity is maintained at temperatures ≤300 °C, for which significant gold remains within the selvedge (as judged by DRIFTS and XPS) and likely strong perturbs the electronic properties of surface Pd ensembles (e.g. destabilising chemisorbed alcohol). Initial rates increase sharply at higher temperature, as additional Au diffuses into the Pd core initiating bulk Au/Pd alloying, and the selvedge becomes Pd-rich. The maximum oxidation rate occurred for 700 °C annealed Au shell–Pd core/TiO_2 NPs, which possess a surface alloy composition ($Au_{40}Pd_{60}$) close to the theoretical limit for complete intermixing and loss of the initial biphasic core–shell structure. This limiting composition is precisely that we recently predicted should be optimal for crotyl alcohol oxidation [11], with additional surface Pd likely to favour undesired decarbonylation. The increased activity upon alloying is closely mirrored by a corresponding rise in selectivity towards crotonaldehyde versus butyraldehyde, from only 50% over the pure gold shell to 85% over the $Au_{40}Pd_{60}$ surface alloy NPs. The poor performance of the initial core–shell structure is somewhat surprising, since monometallic Au particles are generally more selective oxidation catalysts than their monometallic Pd analogues [7]. However, TiO_2-supported Pd nanoparticles do exhibit higher selectivities in the oxidation of glycerol to glycerate and 1,2-propanediol to lactate than corresponding Au/TiO_2 systems [40,41], so there is precedent for our observation. We attribute this higher selectivity following Pd intermixing to stronger oxygen adsorption over Au/Pd alloy surfaces compared with pure gold, resulting in a higher coverage of surface oxygen adatoms, and thus shorter residence time for atomic hydrogen and corresponding reduced tendency for C=C hydrogenation of crotonaldehyde to butyraldehyde. Au/Pd intermixing thus confers both high activity and selectivity in crotyl alcohol selox. Unfortunately, with the 5 layer Au shell initially present in our NPs we cannot generate sufficiently Pd-rich alloys to test whether their selox activity passes through a maximum, as anticipated for limiting alloy compositions ≤35% Au [11,12]. Ongoing work is exploring the effect of changing the dimensions of both Pd core diameter and Au shell thickness on subsequent thermally-induced alloying and catalysis.

4. Conclusions

Nanoengineered bimetallic catalysts offer a great opportunity to test fundamental concepts in heterogeneous catalysis, and to optimise alloy compositions for commercially important reactions over dispersed, high area catalysts. Au shell–Pd core bimetallic nanoparticles have been prepared and dispersed over anatase titania, without loss of structural integrity. Thermal processing gradually induces Pd surface segregation, and is accompanied by both bulk and surface alloying and a concomitant dramatic enhancement in the rate of selective oxidation. Since we have shown the optimal surface and bulk alloy compositions are essentially identical (containing ~40 atom% gold), it should be possible to bypass the core–shell synthetic route and directly prepare high yielding, pre-alloyed $Au_{40}Pd_{60}$ nanocatalysts for this selox reaction.

Acknowledgements

We thank the Engineering and Physical Sciences Research Council for financial support (EP/E046754/1 and EP/G007594/1) and the award of a Leadership Fellowship (A.F.L.) and studentship (C.V.E.). Electron microscopy access was provided through the Leeds EPSRC Nanoscience and Nanotechnology Research Equipment Facility (LENNF) (EP/F056311/1). We also thank Syngenta for additional studentship support and Mr. L. Dingwall (York Chemistry) and

Dr. I. Harvey for assistance with DRIFTS and EXAFS measurements, respectively.

Appendix A. Supplementary data

Supplementary data associated with this article can be found, in the online version, at doi:10.1016/j.cattod.2010.04.032.

References

[1] A.J. Urquhart, F.J. Williams, O.P.H. Vaughan, R.L. Cropley, R.M. Lambert, Chem. Commun. (2005) 1977.
[2] C. Chapuis, D. Jacoby, Appl. Catal. A: Gen. 221 (2001) 93.
[3] A.F. Lee, Z. Chang, P. Ellis, S.F.J. Hackett, K. Wilson, J. Phys. Chem. C 111 (2007) 18844.
[4] S.E.J. Hackett, R.M. Brydson, M.H. Gass, I. Harvey, A.D. Newman, K. Wilson, A.F. Lee, Angew. Chem. Int. Ed. 46 (2007) 8593.
[5] A.F. Lee, S.F.J. Hackett, J.S.J. Hargreaves, K. Wilson, Green Chem. 8 (2006) 549.
[6] D.I. Enache, D. Barker, J.K. Edwards, S.H. Taylor, D.W. Knight, A.F. Carley, G.J. Hutchings, Catal. Today 122 (2007) 407.
[7] D.I. Enache, J.K. Edwards, P. Landon, B. Solsona-Espriu, A.F. Carley, A.A. Herzing, M. Watanabe, C.J. Kiely, D.W. Knight, G.J. Hutchings, Science 311 (2006) 362.
[8] C.Y. Ma, B.J. Dou, J.J. Li, J. Cheng, Q. Hu, Z.P. Hao, S.Z. Qiao, Appl. Catal. B: Environ. 92 (2009) 202.
[9] S. Marx, A. Baiker, J. Phys. Chem. C 113 (2009) 6191.
[10] P.J. Miedziak, Z.R. Tang, T.E. Davies, D.I. Enache, J.K. Bartley, A.F. Carley, A.A. Herzing, C.J. Kiely, S.H. Taylor, G.J. Hutchings, J. Mater. Chem. 19 (2009) 8619.
[11] A.F. Lee, S.F.J. Hackett, G.J. Hutchings, S. Lizzit, J. Naughton, K. Wilson, Catal. Today 145 (2009) 251.
[12] J. Naughton, A.F. Lee, S.M. Thompson, C.P. Vinod, K. Wilson, PCCP 12 (2010) 2670.
[13] H. Remita, A. Etcheberry, J. Belloni, J. Phys. Chem. B 107 (2002) 31.
[14] D. Jana, A. Dandapat, G. De, J. Phys. Chem. C 113 (2009) 9101.
[15] A.F. Lee, C.J. Baddeley, C. Hardacre, R.M. Ormerod, R.M. Lambert, G. Schmid, H. West, J. Phys. Chem. 99 (1995) 6096.
[16] G. Schmid, A. Lehnert, J.O. Malm, J.O. Bovin, Angew. Chem. Int. Ed. Engl. 30 (1991) 874.
[17] http://cars9.uchicago.edu/iffwiki/Ifeffit.
[18] Y. Kuk, L.C. Feldman, P.J. Silverman, Phys. Rev. Lett. 50 (1983) 511.
[19] P. Dash, T. Bond, C. Fowler, W. Hou, N. Coombs, R.W.J. Scott, J. Phys. Chem. C 113 (2009) 12719.
[20] I. Zasada, M.A. Van Hove, Surf. Sci. 457 (2000) L421.
[21] S.J. Mejia-Rosales, C. Fernandez-Navarro, E. Perez-Tijerina, D.A. Blom, L.F. Allard, M. Jose-Yacaman, J. Phys. Chem. C 111 (2007) 1256.
[22] A. Frenkel, Z. Kristall. 222 (2007) 605.
[23] K. Pirkkalainen, R. Serimaa, J. Appl. Crystallogr. 42 (2009) 442.
[24] P.J. Cumpson, M.P. Seah, Surf. Interface Anal. 25 (1997) 430.
[25] Z. Li, O. Furlong, F. Calaza, L. Burkholder, H.C. Poon, D. Saldin, W.T. Tysoe, Surf. Sci. 602 (2008) 1084.
[26] Z. Li, F. Gao, Y. Wang, F. Calaza, L. Burkholder, W.T. Tysoe, Surf. Sci. 601 (2007) 1898.
[27] C.W. Yi, K. Luo, T. Wei, D.W. Goodman, J. Phys. Chem. B 109 (2005) 18535.
[28] D. de Caro, J.S. Bradley, New J. Chem. 22 (1998) 1267.
[29] P.J. Ellis, I.J.S. Fairlamb, S.F.J. Hackett, K. Wilson, A.F. Lee, Angew. Chem. Int. Ed. 49 (2010) 1820.
[30] D. de Caro, J. Kohler, W. Busser, J. Bradley, Macromol. Symp. 156 (2000) 53.
[31] M. Ruff, S. Frey, B. Gleich, R.J. Behm, Appl. Phys. A: Mater. Sci. Process. 66 (1998) S513.
[32] F. Boccuzzi, A. Chiorino, S. Tsubota, M. Haruta, J. Phys. Chem. 100 (1996) 3625.
[33] F. Boccuzzi, A. Chiorino, M. Manzoli, P. Lu, T. Akita, S. Ichikawa, M. Haruta, J. Catal. 202 (2001) 256.
[34] M.A. Bollinger, M.A. Vannice, Appl. Catal. B: Environ. 8 (1996) 417.
[35] Y. Denkwitz, B. Schumacher, G. Kucerova, R.J. Behm, J. Catal. 267 (2009) 78.
[36] J.-D. Grunwaldt, M. Maciejewski, O.S. Becker, P. Fabrizioli, A. Baiker, J. Catal. 186 (1999) 458.
[37] D. Ferri, B. Behzadi, P. Kappenberger, R. Hauert, K.H. Ernst, A. Baiker, Langmuir 23 (2007) 1203.
[38] S. Devarajan, P. Bera, S. Sampath, J. Colloid Interface Sci. 290 (2005) 117.
[39] E. Ozensoy, D.C. Meier, D.W. Goodman, J. Phys. Chem. B 106 (2002) 9367.
[40] N. Dimitratos, J.A. Lopez-Sanchez, J.M. Anthonykutty, G. Brett, A.F. Carley, R.C. Tiruvalam, A.A. Herzing, C.J. Kiely, D.W. Knight, G.J. Hutchings, PCCP Phys. Chem. Chem. Phys. 11 (2009) 4952.
[41] N. Dimitratos, J.A. Lopez-Sanchez, S. Meenakshisundaram, J.M. Anthonykutty, G. Brett, A.F. Carley, S.H. Taylor, D.W. Knight, G.J. Hutchings, Green Chem. 11 (2009) 1209.